

Ab initio amorphous spin Hamiltonian for the description of topological spin textures in FeGe

Temuujin Bayaraa^{1,2*} and Sinéad M. Griffin^{1,2}

¹Materials Sciences Division, Lawrence Berkeley National Laboratory, Berkeley, California, 94720, USA

²Molecular Foundry Division, Lawrence Berkeley National Laboratory, Berkeley, California, 94720, USA

*tbayaraa@lbl.gov

ABSTRACT

Topological spin textures in magnetic materials such as skyrmions and hopfions are interesting manifestations of geometric structures in real materials, concurrently having potential applications as information carriers. In the crystalline systems, the formation of these topological spin textures is well understood as a result of the competition between interactions due to symmetry breaking and frustration. However, in systems without translation symmetry such as amorphous materials, a fundamental understanding of the driving mechanisms of non-trivial spin structures is lacking owing to the structural and interaction complexity in these systems. In this work, we use a suite of first-principles-based calculations to propose a *ab initio* spin Hamiltonian that accurately represents the diversity of structural and magnetic properties in the exemplar amorphous FeGe. Monte Carlo simulations of our amorphous Hamiltonian find emergent skyrmions that are driven by frustrated geometric and magnetic exchange, consistent with those observed in experiment. Moreover, we find that the diversity of local structural motifs results in a large range of exchange interactions, far beyond those found in crystalline materials. Finally, we observe the formation of large-scale emergent structures in amorphous materials, far beyond the relevant interaction length-scale in the systems, suggesting a new route to emergent correlated phases beyond the crystalline limit.

Introduction

Topologically protected spin textures such as skyrmions cannot be continuously transformed into other magnetic structures^{1,2}, embodying an interesting application of concepts in mathematics to physical systems. Such topological objects can be classified by a quantized topological charge, and are robust to perturbations, making them promising for data storage and low-power spintronics^{1,3}. The theoretical understanding of such topological spin textures has been intimately connected to the presence of crystalline symmetries – they primarily form due to the Dzyaloshinskii-Moriya interaction (DMI)^{4,5} caused by inversion symmetry-breaking found in polar crystals, or from spin frustration induced by alternating higher-order Heisenberg exchange interaction between nearest neighbors⁶.

Interestingly, recent experimental studies report findings of topological spin textures in *amorphous* materials such as GdCo⁷, FeGe^{8,9}, Fe₇₈Si₉B₁₃ alloy¹⁰, and Fe/Gd multilayers¹¹. In fact, magnetism in amorphous systems has a long history with both prior theoretical and experimental works exploring the role of coordination number, exchange interactions, and metallic/insulating nature of the amorphous materials on the resulting magnetic properties^{12–38}. Theoretical efforts to understand magnetism in amorphous materials have explored several approaches including constructing minimal models for disordered systems^{25,32–35}, numerical simulations using classical Heisenberg and Ising models^{36–39}, and micromagnetic simulations by assuming magnetic interaction parameters of the crystalline systems or fitting the model to the experimental values^{40,41}. A key assumption across many of these theories is that the distribution of exchange interactions $J(r_{ij})$ is solely a function of the distance between the magnetic pairs and the anisotropy of the system. Efforts to go beyond this homogeneous approximations include the incorporate of the distribution of magnetic moments as characterized from experimental hyperfine fields²⁵.

However, the chemical and structural disorder in amorphous systems leads to a distribution of magnetic properties, especially their exchange interactions, magnetic moments, and single-ion anisotropies. Therefore, a faithful theoretical description of amorphous magnetic systems requires a site-by-site description of the exchange interactions, currently only possible through first-principles-based approaches. With this information, the origin and driving mechanisms behind the formation of spin textures in amorphous systems with their range of chemical and structural distributions can be accurately described. This can also address fundamental questions about their formation such as whether topological spin textures in amorphous materials are formed by DMI as is common in the crystalline systems or local frustration introduced by disorder? Is there a different mechanism contributing to the formation of spin textures in amorphous systems? How do the magnetic properties and magnetic interactions differ in amorphous structures in comparison to their crystalline counterparts?

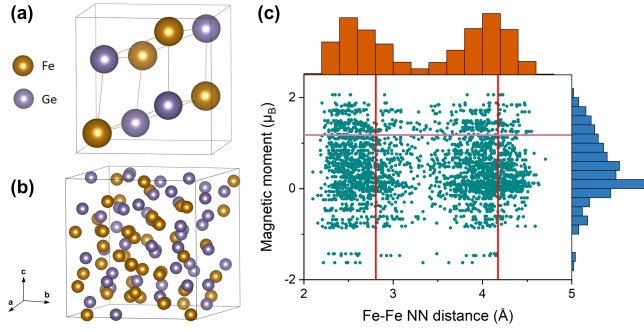


Figure 1. (a) Crystal structure of FeGe in the B20 space group and (b) example amorphous snapshot of 96-atoms FeGe cell. (c) Fe-Fe Nearest-Neighbor (NN) distances and their magnetic moments in five amorphous snapshots considered in this work. Red vertical lines are the 1NN and 2NN distances in the B20 crystal structure and the pink horizontal line represents the magnetic moment of Fe ions in the B20 crystal structure. Histograms on the top and the right show the distribution of Fe-Fe NN distances and magnetic moments, respectively.

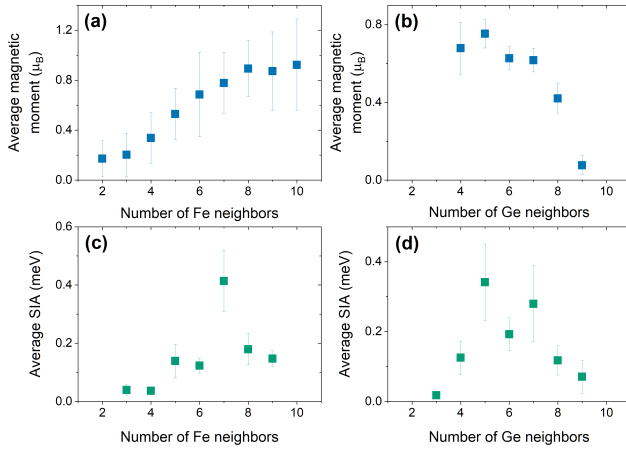


Figure 2. (a,b) The average magnetic moment and (c,d) SIA as a function of the number of Fe and Ge neighbors within 3.5\AA . Error bars are the standard deviation in the magnetic moments with respect to the average magnetic moment of Fe ions.

Here, we provide answers to all these questions by studying the formation of the topological spin textures through the development of an *ab initio* amorphous spin Hamiltonian which is subsequently used for Monte Carlo (MC) simulations. We demonstrate this for amorphous FeGe and compare it to its crystalline counterpart, finding that magnetic exchange coupling parameters can be much stronger in amorphous structures with respect to their crystalline counterparts due to their disordered nature resulting in (i) a distribution of bond lengths including some both shorter and longer than those found in crystalline versions, and (ii) variation in their magnetic moments which, we find, depends on the local coordination environment of each Fe. Furthermore, we reveal that amorphous FeGe structures host nanoscale skyrmion spin textures that are stabilized by the frustrated magnetic exchange coupling coefficients rather than DMI or single-ion-anisotropy. Our results suggest that topological spin textures can be found in amorphous magnetic materials without the presence of strong spin-orbit-coupling or competing long-range interactions and that large-scale emergent magnetic superstructures form beyond the inherent interactions scales in magnetic materials.

Approach

We begin our study with the crystalline B20 FeGe system to benchmark our approach and as a comparison with the amorphous systems. Fig. 1(a) shows the cubic B20 FeGe crystal structure – the observation of magnetic skyrmions and other non-collinear spin structures in the B20 phases of FeGe, MnSi, and $\text{Fe}_{1-x}\text{Co}_x\text{Si}$ have been extensively reported ^{42–44}. Due to the chiral crystal structure, they lack inversion symmetry which permits a nonzero Dzyaloshinskii-Moriya interaction (DMI). The chiral *spin* structures in B20 structures then form due to the competition between Heisenberg exchange interaction and DMI. We calculated

all magnetic interaction parameters between Fe pairs within 10\AA which matches well with previous studies^{45–47} (note that SIA is negligible in crystalline FeGe due to having cubic symmetry and see Supplemental Materials for more details). Using these extracted parameters we performed MC simulations of the spin Hamiltonian of Eqs. (1) and (2) (see Methods section) to study the finite-temperature magnetic properties and potential emergent spin structures. We simulated supercells as large as $40\times 40\times 40$ and found spin textures such as skyrmions that are found experimentally in FeGe thin films^{6,48–51}. However, we did not find chiral spiral spin structures due to the computational limitations and finite size effects of the unit-cell size in our calculations, and we refer to previous works that circumvented this using micromagnetic simulations^{45–47} (see SM).

We now develop an *ab initio* spin Hamiltonian for amorphous FeGe. We begin by generating a series of amorphous snapshots with *ab initio* molecular dynamics (AIMD) through a melt-quench procedure (see Supplemental Materials). This method has been successfully shown to reproduce measured radial distribution functions of amorphous thin films⁵² and so should accurately represent the as-grown atomic structure in our materials. Fig. 1(b) shows an example snapshot of an AIMD-generated amorphous structure comprising $\text{Fe}_{48}\text{Ge}_{48}$. From these amorphous snapshots, we perform Density Functional Theory (DFT) calculations to further relax our amorphous supercells to extract magnetic moments of Fe ions and Fe-Fe Nearest-Neighbor (NN) pair distances. These are reported for five amorphous snapshots and depicted in Fig. 1(c).

Results

We first analyze our calculated amorphous bond length distributions and magnetic moments and compare them with those of the crystalline case. Examining the peaks of the histograms in Fig. 1(c) with respect to the crystalline references (vertical lines for 1NN and 2NN distance and the horizontal line for the magnetic moment), we find that the 1NN distance is reduced ($\sim 2.50\text{\AA}$) with respect to the crystalline case ($\sim 2.88\text{\AA}$). However, the 2NN are very similar in both cases (amorphous is $\sim 4.20\text{\AA}$, and crystalline is $\sim 4.30\text{\AA}$). The right histogram shows that Fe ions can host magnetic moments ranging from $-1.80\mu_B$ to $2.05\mu_B$ with a majority of them being around $0\mu_B$ and the average magnetic moment of Fe ions in the five amorphous snapshots range from $0.52\mu_B$ to $0.79\mu_B$ in the collinear limit which is in good agreement with the experimental average magnetic moment of Fe ions of $0.75\mu_B$ ⁸ (see Table S2). In addition, we find ferromagnetic interactions to be dominant in the studied amorphous structures however we also find some antiferromagnetic interactions resulting in an overall ferrimagnetic ordering in the collinear limit.

To explore the origins of the decrease in the magnitude of the average magnetic moments in amorphous structures ($0.75\mu_B$) compared to the crystalline magnetic moment of $1.1\mu_B$, we examine their local coordination environment. Prior experimental reports find the magnetic moment of amorphous Fe is found to decrease by approximately 20%⁵³, consistent with our theoretical results, and that both non-magnetic and magnetic Fe around found near $x=0.5$ composition of amorphous $\text{Fe}_x\text{Ge}_{1-x}$ and $\text{Fe}_x\text{Si}_{1-x}$ ⁵⁴. To understand this, we plot the average magnetic moment of Fe as a function of both Fe and Ge neighbors in Fig. 2. We find that the average moment increases as a function of the number of Fe neighbors, and decreases with increasing Ge neighbors. This is consistent with experimental findings of the hyperfine fields study having almost linear behavior for the number of Fe-Fe nearest neighbors from 8 to 10 for various compositions of amorphous $\text{Fe}_x\text{Si}_{1-x}$ ⁵⁴. Similar findings were also found in amorphous $\text{Fe}_x\text{Si}_{1-x}$ thin films⁵⁵ where the magnitude of the magnetic moments of Fe was found to decrease with more Si neighbors. These results can be easily understood in the framework of metallic magnetic amorphous materials proposed by²⁵ where the magnitude of magnetic moments in metallic systems is driven by the number of magnetic neighbors, characteristic of the random-dense-packing found in amorphous metals.

We next calculate the single-ion anisotropy on each Fe finding it can reach as large as 0.4 meV (on average). Fig. 2(c,d) shows the average magnitude of the SIA as a function of the number of Fe and Ge neighbors of each Fe site. We report the average of the diagonal elements of the single-ion anisotropy matrix as SIA value. Fig. 2(c) shows that SIA increases with the number of magnetic neighbors. Interestingly, an experimental phase diagram of amorphous FeGe⁸ was recently reported where they find that with increasing Fe concentration, the system goes through low-temperature, helical, and ferromagnetic phases. Since increasing anisotropy generally leads to larger domains⁵⁶, this is consistent with our theoretical results.

We select three amorphous structures depending on their average magnetic moment of Fe ions with respect to the experimental value of $0.75\mu_B$ ⁸ (see Supplemental Materials). Fig. 3 shows the 3D scatter plots of the magnetic exchange couplings (J) and three components of the DMI vectors that we extracted from three amorphous structures (in total, we studied 502 Fe-Fe pairs). We considered all the Fe-Fe pairs within the bond-length of 4.5\AA as we found that the strength of J and DMI becomes negligible above bond-length of $\sim 4\text{\AA}$ (see Fig. S3). We report the J and DMI values as 3D scatter plots as a function of the magnetic moments of each ion of the pairs and their corresponding separation. Interestingly, our results suggest that the assumption that J and DMI only depend on pair distance, $J(r_{ij})$ does not hold in amorphous materials. Indeed we find pairs having different J and DMI values even though with the same separation (see Fig. S3). This is due to different local magnetic environments and the diverse Fe magnetic moments that are dependent on the local coordination environment of each Fe, which is unique for each Fe ion (Fig. 2(a,b)). We find that J increases when both magnetic moments of the Fe pair are large with a shorter separation in Fig. 3(a), reaching up to -362 meV , which is much higher than the crystalline J of -7.5

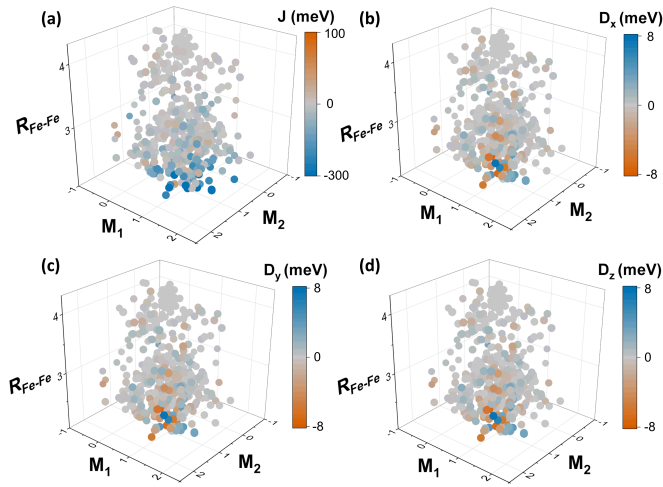


Figure 3. Magnetic exchange couplings (J) and three components of the DMI vectors are shown as 3D scatter plots and with heat-map depending on their strengths. The x and y axes show the magnetic moments (μ_B) of the Fe ions from the pairs. The z-axis is the distance (\AA) between the Fe pairs.

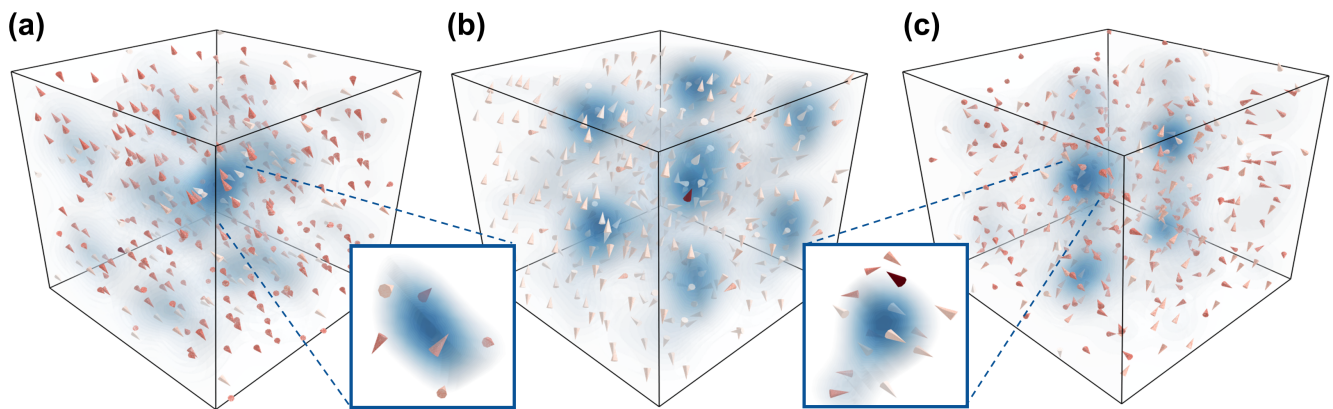


Figure 4. Distribution of topological charge Q in blue colors and spin textures of the supercells of three amorphous FeGe structures possessing 3D spiral spin textures, as found from MC simulations at low temperatures. Arrows represent the spin patterns at each magnetic site in the supercells and the coloring goes to red from white depending on the rotation angle of the spins. The black boxes show the considered supercell.

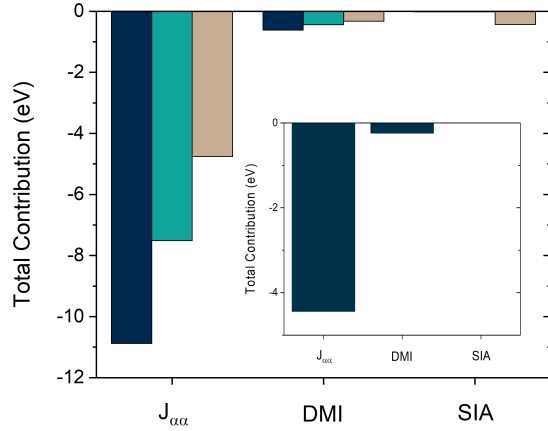


Figure 5. Total related contribution energies of all $J_{\alpha\alpha}$, DMI, and SIA for three amorphous spin textures (in three different colors) shown in Fig. 3. The inset shows the total related contribution energies of $J_{\alpha\alpha}$, DMI, and SIA surrounding the skyrmion at the center of Fig. 3(a) for its formation.

meV. This trend can also be seen in DMI vectors in Fig. 3(b-d) where the DMI magnitudes are found to reach up to 9.4 meV (compared with the crystalline value of 0.5 meV). Averaging the J parameters in the three studied amorphous snapshots gives -9.2, -17.5, and -27.2 meV which are still larger than the crystalline J of -7.5 meV. Similarly, for DMI, we find an average value reaching a magnitude of 0.2 meV which is also large with respect to the crystalline value of 0.45 meV. Fig. 3 shows the importance of magnetic moments, both the magnitude and sign, for the strength of J and DMI, thus, the common assumption of the exchange interaction to be isotropic and only depending on the distance between the pairs, $J(r_{ij})$, does not hold true in an amorphous system which is contradictory to the common assumptions taken in the previous theoretical works^{25,32–39}. Thus we must consider J to be a function of both pair distance and magnetic moment, where now the magnetic exchange coupling takes the form of $J(r_{ij}, m_i, m_j)$ where m_i and m_j are the magnetic moments on each Fe. Increasing the Fe concentration in $\text{Fe}_x\text{Ge}_{1-x}$ amorphous compounds would result in larger Fe magnetic moments due to more magnetic neighbors (see Fig. 2(a)) and stronger exchange interaction between them. Eventually, this should result in a ferromagnetic ground state which was experimentally found to be true when $x > 0.63$ ⁸.

The results of Monte Carlo (MC) simulations performed using the DFT extracted magnetic parameters for the spin Hamiltonian of Eqs. (1) and (2) are shown in Fig. 3 and. We also studied the crystalline structure and results are reported in the SM. Fig 4 shows the spin textures and distribution of topological charge, Q , found in the supercells of three different amorphous structures for low temperatures, $\sim 12\text{K}$, using the definition of Berg and Lüstcher⁵⁷. We find a different distribution of Q for all three amorphous structures and we verified that there are indeed spin spiral textures around the high-density distribution of Q by zooming into the structures (see zoom-ins Fig. 4). Our results show that these 3D spin spiral textures are indeed the skyrmions or Bloch points that are reported to be the low-temperature state of the amorphous FeGe system in Ref.⁸. These spin textures have positive Q and are found to be stable under an external magnetic field up to 10T. The size of the skyrmions was found to vary from $\sim 26\text{\AA}^3$ to $\sim 221\text{\AA}^3$, for example, the size of the skyrmion that is enlarged in Fig. 4(a) is $\sim 5.5\text{\AA} \times 7.3\text{\AA} \times 5.5\text{\AA}$. The distance between skyrmions in Fig. 4(b,c) was found to vary between 10 to 15\AA and Fig. 4(b) shows skyrmions forming a lattice (note that in the amorphous system, there would be different magnetic configurations that will not allow the lattice to form in the entirety of the amorphous system). Such nanometric spin textures are appealing for nanoelectronics and could lead to novel functionality and devices⁵⁸.

Discussion

Now, let us examine the microscopic origin behind the formation of these spin textures in amorphous FeGe structures. For this, we calculate the relative contribution energies of each $J_{\alpha\alpha}$, the diagonal elements of the exchange coupling matrix, DMI, and SIA toward the formation of the spin textures shown in Fig. 4. Fig. 5 reports the total contribution energy of all $J_{\alpha\alpha}$, DMI, and SIA parameters in three amorphous structures represented by three different colors. One can see that $J_{\alpha\alpha}$ is the strongest contributor toward the formation of the spin textures in all three amorphous FeGe structures, followed by DMI. Note that the contribution of SIA is almost negligible however, for the amorphous structure shown in Fig. 4(c) or in beige color

in Fig. 5, the total contribution of SIA is -0.43eV which is larger than DMI value of -0.32eV . These calculations take into account the contributions of all the magnetic interaction parameters and whole spin textures in the amorphous supercells, thus let us verify whether the contribution trend is the same for the spin textures themselves. The inset in Fig. 5 shows the total contributions of $J_{\alpha\alpha}$, DMI, and SIA parameters near the spin texture shown as the zoom-in in Fig. 4(a) and the result shows that indeed the $J_{\alpha\alpha}$ s are the main contributors followed by contributions coming from DMI. To check if one needs DMI for the formation of the spin textures, we ran numerical MC experiments without considering the DMI and starting from the spin textures. Spin textures were found to stay but the topological charge Q distribution became less dense. Unlike, the crystalline structures where DMI or long-range interactions are the main contributors, spin textures in amorphous structures are found to form due to their complicated nearest-neighbor magnetic exchange coupling coefficients. Thus, one could have spin textures in any amorphous magnetic system without inducing strong spin-orbit coupling with heavy elements or frustration induced by competing long-range interactions. This was indeed found to be true and Ref.¹⁰ reports experimental findings of topological spin textures in amorphous $\text{Fe}_{78}\text{Si}_9\text{B}_{13}$ alloy that has no heavy elements.

Outlook

In summary, we developed an *ab initio* amorphous spin Hamiltonian to describe the magnetic and topological spin textures of amorphous FeGe. Our results reveal that, contrary to conventional understanding, the magnetic exchange interactions ($J_{\alpha\alpha}$ and DMI) depend both on the separation between the magnetic species and on their respective magnetic moments. We find a range of magnetic interactions in amorphous systems whose magnitude is highly dependent on the local coordination environment of each ion, and varies from site to site. Based on our MC simulations that incorporated all of this structural and magnetic complexity, we find that topological spin textures are formed due to the isotropic exchange coupling coefficients in contrast with the driving mechanism crystalline systems where it is due to DMI or long-range interactions. Our results further indicate that any magnetic amorphous system could host nanoscale topological spin textures because of their inherent frustrated and disordered structure, and that emergent large-scale features can result. We hope our predictions will motivate further exploration of magnetic amorphous systems and will be put to use to design novel quantum devices.

Methods

All first-principles calculations were carried out within the framework of Density Functional Theory (DFT) as implemented in Vienna *Ab-Initio* Software Package (VASP)⁵⁹ using the projector augmented-wave potentials⁶⁰. For the crystalline case, we used the generalized gradient approximation, with the Perdew-Burke-Ernzerhof exchange-correlation functional^{61,62}, and an effective Hubbard U parameter of 1.5 eV for the localized 4p electrons of the Ge ions. Typically the Hubbard U parameter is introduced on localized manifolds to account for the underlocalization inherent in the mean-field treatment in DFT and is often benchmarked against experimental observations such as lattice parameters and magnetic moments. However, since FeGe is a metal, we do not expect there to be a need for significant corrections of the Fe-d manifold. Interestingly, as was previously reported, a better agreement with experimental lattice parameters for B20 FeGe is obtained with a U on the Ge-4p as discussed in Ref.⁴⁵ (see Table S1 of Supplemental Materials). We selected a Hubbard U value of 1.5 eV to best reproduce the lattice parameters and Fe magnetic moments in experiment⁶³ find the calculated lattice constant, $a = 4.69\text{\AA}$ ($a = 4.69\text{\AA}$ in experiment⁶³), and the magnetic moment of $1.18\mu_B$ per unit cell ($\approx 1\mu_B$ in experiment⁶³).

We used an energy cutoff of 860 eV and a Monkhorst-Pack k-point mesh density of $13 \times 13 \times 13$ and Γ point only sampling for the Brillouin Zone (BZ) of the crystalline and amorphous cases, respectively. All structural relaxations were performed until the Hellmann-Feynman force on each atom was less than 0.001 eV/\AA and included spin-orbit coupling (SOC) self consistently as implemented in VASP. After obtaining optimized crystalline structure, we used *ab-initio* molecular dynamics (AIMD) simulations with the NVT ensemble as implemented in VASP using a time-step of 2 fs. Such ‘melt-quench’ methodology was previously demonstrated on several systems^{52,64–67} and atoms were first randomly distributed in a cubic simulation cell using Packmol package⁶⁸. The supercell size was chosen to contain 96 atoms to balance having a large enough size to obtain representative amorphous environments with a reasonable runtime of AIMD simulations (note that crystalline unit cell has 8 atoms). All our amorphous calculations were for a $\text{Fe}_{0.5}\text{Ge}_{0.5}$ stoichiometry. To obtain a stable liquid phase, the pressure was equilibrated through a series of AIMD simulations at 3000 K, with rescaling of the unit cell between each AIMD simulation until an internal pressure was 0 bar. Afterward, we performed a 10 ps production run after the energy equilibration process, collecting five snapshots of the melted structures at regular intervals. We quenched these five snapshots following a stepped cooling scheme with 400 fs cooling and 1 ps isothermal steps. Our final amorphous structures were optimized using VASP with the higher precision parameters mentioned previously. For the amorphous case, we used the local-density approximation (LDA)⁶⁹ to have the average magnetic moments of the Fe ions closer to the experimental value of $0.75\mu_B$ ⁸ (see Table S2 of Supplemental Materials).

To study the spin textures in both crystalline and amorphous FeGe structures, we construct the following spin Hamiltonian:

$$H = H^{DEC} + H^{DMI} + H^{SIA} \quad (1)$$

with

$$H^{DEC} = \sum_{\langle i,j \rangle} \sum_{\alpha}^{x,y,z} J_{\alpha\alpha} S_i^{\alpha} S_j^{\alpha}$$

$$H^{DMI} = \sum_{\langle i,j \rangle} \mathbf{D} \cdot \mathbf{S}_i \times \mathbf{S}_j \quad (2)$$

$$H^{SIA} = \sum_i \mathbf{S}_i \cdot \mathbf{A}_{ii} \cdot \mathbf{S}_i$$

where H^{DEC} , H^{DMI} , H^{SIA} represent energies from the diagonal exchange coupling, DMI, and single-ion anisotropy (SIA)⁷⁰, respectively. The sum over $\langle i, j \rangle$ and NN denote the different magnetic pairs and nearest-neighbor interactions that are considered here, respectively. For the crystalline structure, we considered all NNs within 10Å, and for the amorphous structures, only 1st NNs within 4.5Å. The sum over i runs through all magnetic sites. Spins (S) are set to be 1 and their values are absorbed by the magnetic exchange coupling (J) parameters. All magnetic parameters in the Eqs. (1) and (2) are obtained from DFT calculations using the 4-state energy mapping method^{71–73} and Green's function method⁷⁴ for the amorphous and crystalline structures, respectively.

Parallel tempering Monte Carlo (MC) simulations^{75,76} with a conjugate gradient (CG) method⁷⁷ were performed using the extracted magnetic parameters and the Hamiltonian of Eqs. (1) and (2), to predict the magnetic properties and spin textures for both the crystalline and amorphous structures. For the crystalline case, different sizes of supercells were considered ranging from 64×64×2 to 40×40×40 to observe different spin textures and, at each temperature, 160,000 Monte Carlo sweeps were performed. For the amorphous case, we performed MC simulations with 2×2×2 supercells of 96-atom cells.

Acknowledgements

We thank Frances Hellman, Peter Fischer, David Raftrey and Guy Moore for useful discussions. This work is supported by the U.S. Department of Energy, Office of Science, Office of Basic Energy Sciences, Materials Sciences and Engineering Division under Contract No. DE-AC02-05-CH11231 within the Nonequilibrium Magnetic Materials Program (MSMAG). Computational resources were provided by the National Energy Research Scientific Computing Center and the Molecular Foundry, DOE Office of Science User Facilities supported by the Office of Science, U.S. Department of Energy under Contract No. DEAC02-05CH11231. The work performed at the Molecular Foundry was supported by the Office of Science, Office of Basic Energy Sciences, of the U.S. Department of Energy under the same contract.

References

1. Fert, A., Reyren, N. & Cros, V. Magnetic skyrmions: advances in physics and potential applications. *Nat. Rev. Mater.* **2017** 2:7 **2**, 1–15, DOI: [10.1038/natrevmats.2017.31](https://doi.org/10.1038/natrevmats.2017.31) (2017).
2. Griffin, S. M. & Spaldin, N. A. On the relationship between topological and geometric defects. *J. Physics: Condens. Matter* **29**, 343001 (2017).
3. Sampaio, J., Cros, V., Rohart, S., Thiaville, A. & Fert, A. Nucleation, stability and current-induced motion of isolated magnetic skyrmions in nanostructures. *Nat. Nanotechnol.* **2013** 8:11 **8**, 839–844, DOI: [10.1038/nnano.2013.210](https://doi.org/10.1038/nnano.2013.210) (2013).
4. Dzyaloshinsky, I. A thermodynamic theory of “weak” ferromagnetism of antiferromagnetics. *J. Phys. Chem. Solids* **5**, 1259, DOI: [10.1016/0022-3697\(58\)90076-3](https://doi.org/10.1016/0022-3697(58)90076-3) (1957).
5. Moriya, T. Anisotropic superexchange interaction and weak ferromagnetism. *Phys. Rev.* **120**, 91–98, DOI: [10.1103/PhysRev.120.91](https://doi.org/10.1103/PhysRev.120.91) (1960).
6. Zhang, S. L. *et al.* Room-temperature helimagnetism in FeGe thin films. *Sci. Reports* **7**, 123, DOI: [10.1038/s41598-017-00201-z](https://doi.org/10.1038/s41598-017-00201-z) (2017).
7. Streubel, R. *et al.* Experimental Evidence of Chiral Ferrimagnetism in Amorphous GdCo Films. *Adv. Mater.* **30**, 1800199, DOI: [10.1002/adma.201800199](https://doi.org/10.1002/adma.201800199) (2018).
8. Streubel, R. *et al.* Chiral Spin Textures in Amorphous Iron–Germanium Thick Films. *Adv. Mater.* **33**, 2004830, DOI: [10.1002/adma.202004830](https://doi.org/10.1002/adma.202004830) (2021).

9. Singh, A. *et al.* Characterizing Temporal Heterogeneity by Quantifying Nanoscale Fluctuations in Amorphous Fe-Ge Magnetic Films. *Adv. Funct. Mater.* **33**, 2300224, DOI: [10.1002/adfm.202300224](https://doi.org/10.1002/adfm.202300224) (2023).
10. Wu, W. *et al.* Ultra-small topological spin textures with size of 1.3nm at above room temperature in Fe₇₈Si₉B₁₃ amorphous alloy (2023).
11. Montoya, S. A., Lubarda, M. V. & Lomakin, V. Transport properties of dipole skyrmions in amorphous Fe/Gd multilayers. *Commun. Phys.* **5**, 293, DOI: [10.1038/s42005-022-01073-0](https://doi.org/10.1038/s42005-022-01073-0) (2022). [2208.08487](https://doi.org/10.1038/s42005-022-01073-0).
12. Mizoguchi, T. Magnetism in Amorphous Alloys. In *AIP Conference Proceedings*, vol. 34, 286–291, DOI: [10.1063/1.2946104](https://doi.org/10.1063/1.2946104) (AIP Publishing, 1976).
13. Chappert, J., Arrese-Boggiano, R. & Coey, J. Appearance of magnetism in amorphous Y_{1-x}Fe_x. *J. Magn. Magn. Mater.* **7**, 175–177, DOI: [10.1016/0304-8853\(78\)90175-0](https://doi.org/10.1016/0304-8853(78)90175-0) (1978).
14. Lee, K. & Heiman, N. Magnetism in rare earth-transition metal amorphous alloy films. In *AIP Conference Proceedings*, vol. 24, 108–109, DOI: [10.1063/1.30004](https://doi.org/10.1063/1.30004) (AIP, 1975).
15. Cochrane, R. W., Ström-Olsen, J., Williams, G., Liénard, A. & Rebouillat, J. P. Magnetic and transport properties of amorphous NiY and FeY. *J. Appl. Phys.* **49**, 1677–1679, DOI: [10.1063/1.324885](https://doi.org/10.1063/1.324885) (1978).
16. Sherrington, D. & Kirkpatrick, S. Solvable Model of a Spin-Glass. *Phys. Rev. Lett.* **35**, 1792–1796, DOI: [10.1103/PhysRevLett.35.1792](https://doi.org/10.1103/PhysRevLett.35.1792) (1975).
17. Handrich, K. A Simple Model for Amorphous and Liquid Ferromagnets. *physica status solidi (b)* **32**, K55–K58, DOI: [10.1002/pssb.19690320166](https://doi.org/10.1002/pssb.19690320166) (1969).
18. Binder, K. & Stauffer, D. Monte Carlo simulation of a three-dimensional spin glass. *Phys. Lett. A* **57**, 177–179, DOI: [10.1016/0375-9601\(76\)90206-1](https://doi.org/10.1016/0375-9601(76)90206-1) (1976).
19. Walker, L. R. & Walstedt, R. E. Computer Model of Metallic Spin-Glasses. *Phys. Rev. Lett.* **38**, 514–518, DOI: [10.1103/PhysRevLett.38.514](https://doi.org/10.1103/PhysRevLett.38.514) (1977).
20. Litterst, F. Susceptibility of non-crystalline ferromagnetic FeF₂. *J. de Physique Lettres* **36**, 197–199, DOI: [10.1051/jphyslet:01975003607-8019700](https://doi.org/10.1051/jphyslet:01975003607-8019700) (1975).
21. Lines, M. E. A computer model for amorphous Fe $\langle \mathbf{F} \rangle$. *Phys. Rev. B* **21**, 5793–5801, DOI: [10.1103/PhysRevB.21.5793](https://doi.org/10.1103/PhysRevB.21.5793) (1980).
22. Moorjani, Kishin, Coey, J. M. D. Magnetic glasses. *Elsevier* (1984).
23. Buschow, K. On the difference in the magnetic properties of amorphous alloys and intermetallic compounds. *J. Magn. Magn. Mater.* **28**, 20–28, DOI: [10.1016/0304-8853\(82\)90025-7](https://doi.org/10.1016/0304-8853(82)90025-7) (1982).
24. Coey, J. M. D., Ryan, D. H. & Boliang, Y. Influence of hydrogen on the magnetic properties of iron-rich metallic glasses (invited). *J. Appl. Phys.* **55**, 1800–1804, DOI: [10.1063/1.333483](https://doi.org/10.1063/1.333483) (1984).
25. Coey, J. M. D. Amorphous magnetic order. *J. Appl. Phys.* **49**, 1646–1652, DOI: [10.1063/1.324880](https://doi.org/10.1063/1.324880) (1978).
26. Chappert, J., Coey, J. M. D., Lienard, A. & Rebouillat, J. P. Amorphous yttrium-iron alloys. II. Mossbauer spectra. *J. Phys. F: Met. Phys.* **11**, 2727–2744, DOI: [10.1088/0305-4608/11/12/019](https://doi.org/10.1088/0305-4608/11/12/019) (1981).
27. Masumoto, T., Ohnuma, S., Shirakawa, K., Nose, M. & Kobayashi, K. MAGNETIC PROPERTIES OF METAL-METAL AMORPHOUS ALLOYS. *Le J. de Physique Colloques* **41**, C8–686–C8–689, DOI: [10.1051/jphyscol:19808172](https://doi.org/10.1051/jphyscol:19808172) (1980).
28. Fujimori, H., Nakanishi, K., Hiroyoshi, H. & Kazama, N. S. Magnetic and thermal expansion properties in hydrided Fe–Zr amorphous alloys. *J. Appl. Phys.* **53**, 7792–7794, DOI: [10.1063/1.330208](https://doi.org/10.1063/1.330208) (1982).
29. Coey, J. M. *et al.* Amorphous yttrium-iron alloys: III. The influence of hydrogen. *J. Phys. F: Met. Phys.* **18**, 1299, DOI: [10.1088/0305-4608/18/6/030](https://doi.org/10.1088/0305-4608/18/6/030) (1988).
30. Kaneyoshi, T. *Amorphous Magnetism* (CRC Press, 2018).
31. COEY & DAVID, J. M. Current trends in amorphous magnetism. *IEEE TRANSACTIONS ON MAGNETICS* **20** (1984).
32. Petrakovskii, G. A. Amorphous magnetic materials. *Sov. Phys. Uspekhi* **24**, 511–525, DOI: [10.1070/PU1981v024n06ABEH004850](https://doi.org/10.1070/PU1981v024n06ABEH004850) (1981).
33. Aharony, A. Critical behavior of amorphous magnets. *Phys. Rev. B* **12**, 1038–1048, DOI: [10.1103/PhysRevB.12.1038](https://doi.org/10.1103/PhysRevB.12.1038) (1975).

34. Kaneyoshi, T. *Introduction to Amorphous Magnets* (WORLD SCIENTIFIC, 1992).
35. Kaneyoshi, T. *Amorphous Magnetism* (CRC Press; 1st edition (November 29, 2017), 2017).
36. Belokon, V., Lapenkov, R. & Dyachenko, O. Magnetic phase transition in an amorphous alloy: The theory of random fields of exchange interaction. *J. Magn. Magn. Mater.* **564**, 170172, DOI: [10.1016/j.jmmm.2022.170172](https://doi.org/10.1016/j.jmmm.2022.170172) (2022).
37. Santos-Filho, J. B., Plascak, J. A. & Landau, D. P. Monte carlo study of the phase diagram of disordered Fe_pAl_{1-p} alloys: A site-diluted isotropic heisenberg model. *Phys. Rev. B* **103**, 024446, DOI: [10.1103/PhysRevB.103.024446](https://doi.org/10.1103/PhysRevB.103.024446) (2021).
38. Plascak, J. A., Zamora, L. E. & Pérez Alcazar, G. A. Ising model for disordered ferromagnetic Fe – Al alloys. *Phys. Rev. B* **61**, 3188–3191, DOI: [10.1103/PhysRevB.61.3188](https://doi.org/10.1103/PhysRevB.61.3188) (2000).
39. Fähnle, M. Monte Carlo study of phase transitions in bond- and site-disordered Ising and classical Heisenberg ferromagnets. *J. Magn. Magn. Mater.* **45**, 279–287, DOI: [10.1016/0304-8853\(84\)90019-2](https://doi.org/10.1016/0304-8853(84)90019-2) (1984).
40. Savchenko, A. S. *et al.* Diversity of states in a chiral magnet nanocylinder. *APL Mater.* **10**, 61110, DOI: [10.1063/5.0097650](https://doi.org/10.1063/5.0097650) (2022).
41. Ma, C. T., Xie, Y., Sheng, H., Ghosh, A. W. & Poon, S. J. Robust Formation of Ultrasmall Room-Temperature Néel Skyrmions in Amorphous Ferrimagnets from Atomistic Simulations. *Sci. Reports* **9**, 9964, DOI: [10.1038/s41598-019-46458-4](https://doi.org/10.1038/s41598-019-46458-4) (2019).
42. Moskvina, E. *et al.* Complex Chiral Modulations in FeGe Close to Magnetic Ordering. *Phys. Rev. Lett.* **110**, 077207, DOI: [10.1103/PhysRevLett.110.077207](https://doi.org/10.1103/PhysRevLett.110.077207) (2013).
43. Yu, X. Z. *et al.* Real-space observation of a two-dimensional skyrmion crystal. *Nature* **465**, 901–904, DOI: [10.1038/nature09124](https://doi.org/10.1038/nature09124) (2010).
44. Muhlbauer, S. *et al.* Skyrmion Lattice in a Chiral Magnet. *Science* **323**, 915–919, DOI: [10.1126/science.1166767](https://doi.org/10.1126/science.1166767) (2009). [0902.1968](https://doi.org/10.1038/09021968).
45. Grytsiuk, S. *et al.* Ab initio analysis of magnetic properties of the prototype B20 chiral magnet FeGe. *Phys. Rev. B* **100**, 214406, DOI: [10.1103/PhysRevB.100.214406](https://doi.org/10.1103/PhysRevB.100.214406) (2019). [1909.13545](https://arxiv.org/abs/1909.13545).
46. Grytsiuk, S. & Blügel, S. Micromagnetic description of twisted spin spirals in the B20 chiral magnet FeGe from first principles. *Phys. Rev. B* **104**, 064420, DOI: [10.1103/PhysRevB.104.064420](https://doi.org/10.1103/PhysRevB.104.064420) (2021). [2103.09800](https://arxiv.org/abs/2103.09800).
47. Borisov, V. *et al.* Heisenberg and anisotropic exchange interactions in magnetic materials with correlated electronic structure and significant spin-orbit coupling. *Phys. Rev. B* **103**, 174422, DOI: [10.1103/PhysRevB.103.174422](https://doi.org/10.1103/PhysRevB.103.174422) (2021). [2011.08209](https://arxiv.org/abs/2011.08209).
48. Turgut, E., Stolt, M. J., Jin, S. & Fuchs, G. D. Topological spin dynamics in cubic FeGe near room temperature. *J. Appl. Phys.* **122**, 183902, DOI: [10.1063/1.4997013](https://doi.org/10.1063/1.4997013) (2017). [1705.03397](https://arxiv.org/abs/1705.03397).
49. Zheng, F. *et al.* Experimental observation of chiral magnetic bobbars in B20-type FeGe. *Nat. Nanotechnol.* **13**, 451–455, DOI: [10.1038/s41565-018-0093-3](https://doi.org/10.1038/s41565-018-0093-3) (2018).
50. Kovács, A., Li, Z.-A., Caron, J. & Dunin-Borkowski, R. Magnetic imaging of skyrmions in $\langle scp \rangle FeGe \langle /scp \rangle$ using off-axis electron holography. In *European Microscopy Congress 2016: Proceedings*, 739–740, DOI: [10.1002/9783527808465.EMC2016.6276](https://doi.org/10.1002/9783527808465.EMC2016.6276) (Wiley, 2016).
51. Yu, X. Z. *et al.* Near room-temperature formation of a skyrmion crystal in thin-films of the helimagnet FeGe. *Nat. Mater.* **10**, 106–109, DOI: [10.1038/nmat2916](https://doi.org/10.1038/nmat2916) (2011).
52. Harrelson, T. F. *et al.* Elucidating the local atomic and electronic structure of amorphous oxidized superconducting niobium films. *Appl. Phys. Lett.* **119**, 50, DOI: [10.1063/5.0069549](https://doi.org/10.1063/5.0069549) (2021). [2111.11590](https://arxiv.org/abs/2111.11590).
53. Felsch, W. Ferromagnetismus von amorphem Eisen. *Zeitschrift für Physik A Hadron. nuclei* **219**, 280–299, DOI: [10.1007/BF01397570](https://doi.org/10.1007/BF01397570) (1969).
54. MARCHAL, G., MANGIN, P., PIECUCH, M. & JANOT, C. MÖSSBAUER STUDY OF MAGNETIC ORDERING IN AMORPHOUS Fe-Si ALLOYS. *Le J. de Physique Colloques* **37**, C6–763–C6–768, DOI: [10.1051/jphyscol:19766160](https://doi.org/10.1051/jphyscol:19766160) (1976).
55. Karel, J. *et al.* Using structural disorder to enhance the magnetism and spin-polarization in $Fe_{0.5}Si_{1-x}$ thin films for spintronics. *Mater. Res. Express* **1**, 026102, DOI: [10.1088/2053-1591/1/2/026102](https://doi.org/10.1088/2053-1591/1/2/026102) (2014).
56. Zhang, H. *et al.* Room-temperature skyrmion lattice in a layered magnet (Fe_{0.5}Co_{0.5})₂GeTe. *Sci. Adv.* **8**, 7103, DOI: [10.1126/sciadv.abm7103](https://doi.org/10.1126/sciadv.abm7103) (2022).

57. Berg, B. & Lüscher, M. Definition and statistical distributions of a topological number in the lattice $O(3)$ σ -model. *Nucl. Physics, Sect. B* **190**, 412–424, DOI: [10.1016/0550-3213\(81\)90568-X](https://doi.org/10.1016/0550-3213(81)90568-X) (1981).
58. Seidel, J. Nanoelectronics based on topological structures, DOI: [10.1038/s41563-019-0301-z](https://doi.org/10.1038/s41563-019-0301-z) (2019).
59. Kresse, G. & Joubert, D. From ultrasoft pseudopotentials to the projector augmented-wave method. *Phys. Rev. B* **59**, 1758–1775, DOI: [10.1103/PhysRevB.59.1758](https://doi.org/10.1103/PhysRevB.59.1758) (1999).
60. Blöchl, P. E. Projector augmented-wave method. *Phys. Rev. B* **50**, 17953–17979, DOI: [10.1103/PhysRevB.50.17953](https://doi.org/10.1103/PhysRevB.50.17953) (1994).
61. Liechtenstein, A. I., Anisimov, V. I. & Zaanen, J. Density-functional theory and strong interactions: Orbital ordering in Mott-Hubbard insulators. *Phys. Rev. B* **52**, R5467–R5470, DOI: [10.1103/PhysRevB.52.R5467](https://doi.org/10.1103/PhysRevB.52.R5467) (1995).
62. Perdew, J. P., Burke, K. & Ernzerhof, M. Generalized Gradient Approximation Made Simple. *Phys. Rev. Lett.* **77**, 3865–3868, DOI: [10.1103/PhysRevLett.77.3865](https://doi.org/10.1103/PhysRevLett.77.3865) (1996).
63. Lebech, B., Bernhard, J. & Freltoft, T. Magnetic structures of cubic FeGe studied by small-angle neutron scattering. *J. Physics: Condens. Matter* **1**, 6105–6122, DOI: [10.1088/0953-8984/1/35/010](https://doi.org/10.1088/0953-8984/1/35/010) (1989).
64. Corbae, P. *et al.* Observation of spin-momentum locked surface states in amorphous Bi₂Se₃. *Nat. Mater.* **22**, 200–206, DOI: [10.1038/s41563-022-01458-0](https://doi.org/10.1038/s41563-022-01458-0) (2023). [1910.13412](https://doi.org/10.1038/s41563-022-01458-0).
65. Cheng, J., Sivonxay, E. & Persson, K. A. Evaluation of Amorphous Oxide Coatings for High-Voltage Li-Ion Battery Applications Using a First-Principles Framework. *ACS Appl. Mater. & Interfaces* **12**, 35748–35756, DOI: [10.1021/acsami.0c10000](https://doi.org/10.1021/acsami.0c10000) (2020).
66. Sivonxay, E., Aykol, M. & Persson, K. A. The lithiation process and Li diffusion in amorphous SiO_2 and Si from first-principles. *Electrochimica Acta* **331**, 135344, DOI: [10.1016/j.electacta.2019.135344](https://doi.org/10.1016/j.electacta.2019.135344) (2020).
67. Sivonxay, E. & Persson, K. A. Density functional theory assessment of the lithiation thermodynamics and phase evolution in si-based amorphous binary alloys. *Energy Storage Mater.* **53**, 42–50, DOI: [10.1016/j.enstm.2022.08.015](https://doi.org/10.1016/j.enstm.2022.08.015) (2022).
68. Martínez, L., Andrade, R., Birgin, E. G. & Martínez, J. M. Packmol: A package for building initial configurations for molecular dynamics simulations. *J. Comput. Chem.* **30**, 2157–2164, DOI: [10.1002/jcc.21224](https://doi.org/10.1002/jcc.21224) (2009).
69. Perdew, J. P. & Zunger, A. Self-interaction correction to density-functional approximations for many-electron systems. *Phys. Rev. B* **23**, 5048–5079, DOI: [10.1103/PhysRevB.23.5048](https://doi.org/10.1103/PhysRevB.23.5048) (1981).
70. Xu, Y., Yang, G.-L., Chu, D.-P. & Zhai, H.-R. Theory of the Single Ion Magnetocrystalline Anisotropy of 3d Ions. *physica status solidi (b)* **157**, 685–693, DOI: [10.1002/PSSB.2221570221](https://doi.org/10.1002/PSSB.2221570221) (1990).
71. Xiang, H., Lee, C., Koo, H.-J., Gong, X. & Whangbo, M.-H. Magnetic properties and energy-mapping analysis. *Dalton Trans.* **42**, 823–853, DOI: [10.1039/C2DT31662E](https://doi.org/10.1039/C2DT31662E) (2013).
72. Xu, C., Xu, B., Dupé, B. & Bellaiche, L. Magnetic interactions in BiFeO₃: A first-principles study. *Phys. Rev. B* **99**, 104420, DOI: [10.1103/PhysRevB.99.104420](https://doi.org/10.1103/PhysRevB.99.104420) (2019).
73. Bayaraa, T., Xu, C. & Bellaiche, L. Magnetization Compensation Temperature and Frustration-Induced Topological Defects in Ferrimagnetic Antiperovskite Mn_4N . *Phys. Rev. Lett.* **127**, 217204, DOI: [10.1103/PhysRevLett.127.217204](https://doi.org/10.1103/PhysRevLett.127.217204) (2021).
74. He, X., Helbig, N., Verstraete, M. J. & Bousquet, E. TB2J: A python package for computing magnetic interaction parameters. *Comput. Phys. Commun.* **264**, 107938, DOI: [10.1016/j.cpc.2021.107938](https://doi.org/10.1016/j.cpc.2021.107938) (2021). [2009.01910](https://arxiv.org/abs/2009.01910).
75. Miyatake, Y., Yamamoto, M., Kim, J. J., Toyonaga, M. & Nagai, O. On the implementation of the 'heat bath' algorithms for Monte Carlo simulations of classical Heisenberg spin systems. *J. Phys. C: Solid State Phys.* **19**, 2539–2546, DOI: [10.1088/0022-3719/19/14/020](https://doi.org/10.1088/0022-3719/19/14/020) (1986).
76. Lou, F. *et al.* PASP: Property analysis and simulation package for materials. *The J. Chem. Phys.* **154**, 114103, DOI: [10.1063/5.0043703](https://doi.org/10.1063/5.0043703) (2021).
77. Hestenes, M. & Stiefel, E. Methods of conjugate gradients for solving linear systems. *J. Res. Natl. Bureau Standards* **49**, 409, DOI: [10.6028/jres.049.044](https://doi.org/10.6028/jres.049.044) (1952).

Ab initio amorphous spin Hamiltonian for the description of topological spin textures in FeGe

Temuujin Bayaraa^{1,2*} and Sinéad M. Griffin^{1,2}

¹Materials Sciences Division, Lawrence Berkeley National Laboratory, Berkeley, California, 94720, USA

²Molecular Foundry Division, Lawrence Berkeley National Laboratory, Berkeley, California, 94720, USA

*tbayaraa@lbl.gov

ABSTRACT

The purpose of this Supplemental Material is to report our result on the crystalline FeGe structure and give additional information on the magnetic properties of amorphous structures.

Calculation parameters

Table S1 reports the calculated lattice parameter a and magnetic moment of Fe ions for different Hubbard U parameters applied using the Dudarev approximation on 3d and 2p orbitals of Fe and Ge ions, respectively. Experimental results² are also shown to provide a comparison. We find that larger U values on Fe-d leads to a much larger magnetic moments that those reported in experiment, for instance, a U value of 1.5eV gives $2.27\mu_B$ which is more than double the experimental result of $1\mu_B$. On the other hand, introducing Hubbard U on Ge-p brings the lattice parameters in closer agreement to experiment without enhancing the magnitude of magnetic moments of Fe ions. For example, for a U of 1.5eV on Ge-p, we calculate the lattice parameter and magnetic moment to be 4.69\AA and $1.19\mu_B$ which is in good agreement with the experimental result of 4.69\AA and $1.00\mu_B$ at 10K². A similar finding was reported previously in Ref.² that applying the Hubbard- U correction ($U = 1.5$ eV and $J = 0.5$ eV) to Ge p-orbitals was found to better reproduce the experimentally measured magnetic moments of Fe. However, they found that such Hubbard U treatment increases the length of the spin spiral found in FeGe. Thus, we chose to apply Hubbard U of 1.5eV on 4p orbitals of Ge ions throughout the study of crystalline FeGe structure in the manuscript and hereafter.

Table S1. Lattice parameter and magnetic moment of Fe using different Hubbard U parameters on 3d and 2p orbitals of Fe and Ge, respectively.

	Lattice parameter (\AA)		Magnetic moment (μ_B)
U on Fe (eV)			
	0.5	4.67	1.30
	1.0	4.70	1.73
	1.5	4.77	2.27
U on Ge (eV)			
	1.0	4.68	1.18
	1.5	4.69	1.19
	2.0	4.70	1.19
Without U		4.66	1.17
Exp. results ²		4.69	1.00
Other theory ²		4.67	1.16

Table S2. Comparison of different functionals on lattice parameters and magnetic moments

	Method	Lattice parameter (\AA)	Magnetic moment (μ_B)
Without U	PBE	4.66	1.17
	LDA	4.55	1.11
With U of	PBE	4.69	1.18
1.5eV on Ge	LDA	4.58	1.10
Exp. results ²		4.69	1.00

Table S3. Calculated average magnetic moments of Fe ions in amorphous structures

Amorphous snapshots	PBE (μ_B)	LDA (μ_B)
1	1.41	0.66
2	1.07	0.52
3	1.49	0.57
4	1.55	0.57
5	1.53	0.79
Exp. results [?]	0.75	

We also check the effect of different exchange-correlation functionals such as LDA[?] and PBE[?] on the lattice parameters and magnetic moments. Results are shown in Table S2 and overall both functionals underestimate the lattice parameter but overestimate the magnetic moment of the experimental values[?] and it is in good agreement with previous study[?].

The calculated average magnetic moments of Fe ions in five amorphous snapshots acquired from AIMD calculations using LDA[?] and PBE[?] exchange-correlation functionals are shown in Table S3. The average magnetic moments of Fe ions are found to be about twice the experimental value of $0.75\mu_B$ [?] when PBE exchange-correlation functional was used. On the other hand, when using LDA exchange-correlation functional, the average magnetic moments of Fe ions are calculated to be smaller than the ones PBE generated but much closer to the experimental value. For instance, one of the snapshots was calculated to have the average magnetic moment of $0.79\mu_B$ which is in good agreement with the experimental value of $0.75\mu_B$ [?]. To understand the difference in magnetic moments when using PBE and LDA functionals, we calculated the average Fe-Ge bond lengths. The average Fe-Ge bond lengths are found to be 2.59\AA and 2.54\AA for PBE and LDA functionals, respectively. Thus, when PBE functional is used, Fe *d*-orbitals get more localized, and larger magnetic moments are predicted from the calculations with respect to the case when LDA functional is used. Based on these results, we chose to use LDA exchange-correlation functional for the study of amorphous structures in our manuscript and hereafter. Note that in the crystalline case, both LDA and PBE functionals overestimate the experimental magnetic moment, and in fact, PBE predicts a larger magnetic moment than the one from LDA functional. In addition, Ref.[?] reports the helical spin spiral period is overestimated by a factor of two when using the parameters obtained by both PBE and LDA functionals. Plus, the LDA functional was generally found to work well for amorphous silicates and oxides[?].

Fig. S1 plots the calculated magnetic exchange coupling coefficient (a) and three components of DMI (b-d) as a function of the Fe-Fe pair distance for B20 FeGe. All parameters are calculated using the Green's function method[?] after obtaining Wannier functions. The *ab initio* DFT Bloch wavefunction was projected onto highly symmetric atomic-orbital-like Wannier functions[?] as implemented in VASP code. We included the outermost d orbitals for Fe and p orbitals for Ge to cover the full band overlap from the *ab initio* and Wannier functions. We find the 1NN interaction to be FM, followed by AFM 2NN and 3NN interactions. We find that longer range interactions than these are mostly FM (see Fig. S1(a)). These competing magnetic interactions at different ranges result in geometrically frustrated spin interactions. Moreover, our results of J and DMI match well with previous studies^{?,?,?}.

Using the extracted magnetic parameters and spin Hamiltonian of Eqs. (1 and 2) from the manuscript, we ran Parallel tempering Monte Carlo (MC) simulations^{?,?} with a conjugate gradient (CG) method[?]. We used supercells of different size for the crystalline structures, $64\times 64\times 2$, $128\times 128\times 4$, $24\times 24\times 24$, and $40\times 40\times 40$, and at each temperature, 160,000 Monte Carlo sweeps were performed. Note that $40\times 40\times 40$ supercell is the largest supercell we could run with MC simulation due to the computational limitations. The predicted Curie temperature, T_C , was 235K for $40\times 40\times 40$ supercell which was lower than the experimental value of $\sim 280\text{K}$ [?] and we found T_C increasing with larger supercell sizes thus reaching experimental T_C of 280K is possible if one could consider large enough supercell in their simulations. We found different spin textures from the MC simulations some of which were in good comparison with the experimental results^{?,?,?,?,?}. Note that we were not able to get clear helical spin spiral textures due to the finite size effect and computational limitations. Fig.S2 shows the simulated spin textures of skyrmions (a) from $64\times 64\times 2$ supercell and chiral spin texture (b) from $40\times 40\times 40$ supercell in B20 FeGe. Fig.S2(b) shows a sign of chiral spin texture at the center which hints toward finding a clear helical spin spiral phase over a longer period if larger supercells can be considered in the MC simulations. Thus, finding an experimentally observed helical phase in B20 FeGe structure is possible if one can overcome the finite size effect or computational limitations in MC simulations.

Amorphous magnetic interactions

Fig.S3 shows the calculated magnetic exchange coupling coefficient (a) and three components of DMI (b-d) as a function of the Fe-Fe pair distance for the studied three amorphous FeGe structures. One can see that these parameters can no longer be shown

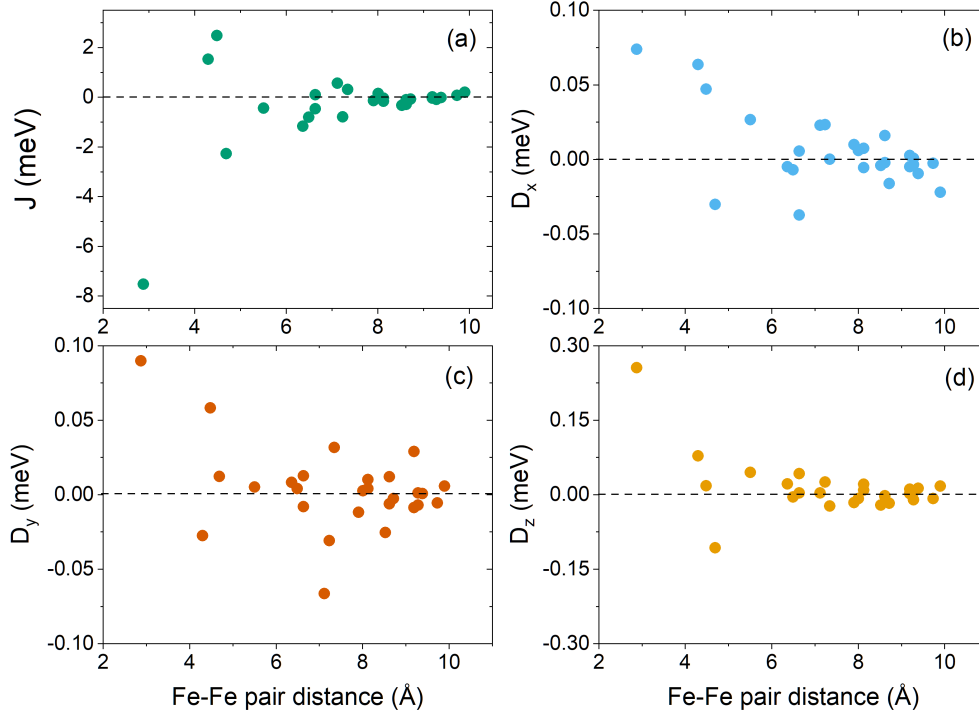


Figure S1. Calculated magnetic exchange coupling (a) and three components of the DMI (b-d) of crystalline FeGe are shown as a function of the Fe-Fe pair distances.

as a function of the Fe-Fe pair distance, as shown here, at the same Fe-Fe pair distance, there are multiple different values of J and DMI. Thus, we show J and DMI values as 3D scatter plots that depend on the magnetic moments of the pairs and their distance from each other in the manuscript. Furthermore, Fig.S3 reveals that J and DMI values widely diversified as Fe-Fe pair distance gets smaller and the effect is larger if the distance becomes smaller than 1NN distance of the crystalline counterpart which is shown as a vertical red dashed line. The horizontal lines in Fig.S3 represent the corresponding J and DMI values of the crystalline structure, as one can see, J and DMI values in amorphous structures are found to be gigantic compared to the crystalline values. However, note that in amorphous structures, there is no symmetry, thus to get the total energy of the spin Hamiltonian, one needs to add each J and DMI contributions separately. On the other hand, the crystalline structures have symmetry and each contribution to the total energy from NN interactions needs to be multiplied by the symmetry elements, in this case, B20 structure has cubic symmetry, and each NN interaction needs to be considered 12 times.

Next, to check whether there is superexchange interaction in amorphous FeGe, we take into account Fe-Ge-Ge angle by finding the closest Ge ion between all the Fe pairs we studied to get their interaction parameters, and the results are shown in Fig.S4. J as a function of the Fe-Ge-Fe angle is plotted. One can see that there is no linear correlation between J and Fe-Ge-Fe angle, in fact, metallic amorphous systems should have either direct exchange coupling or in-direct RKKY interactions as mentioned in Ref.[?]

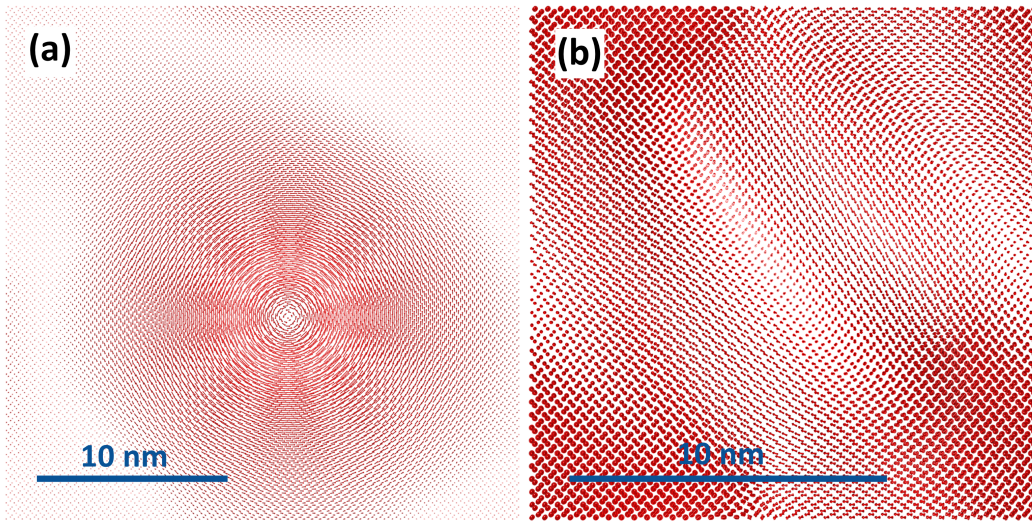


Figure S2. Simulated spin textures of crystalline FeGe (a) and under external magnetic field (b) are shown. To clearly show the skyrmion texture, the studied supercell is extended by 2 times along the in-plane directions.

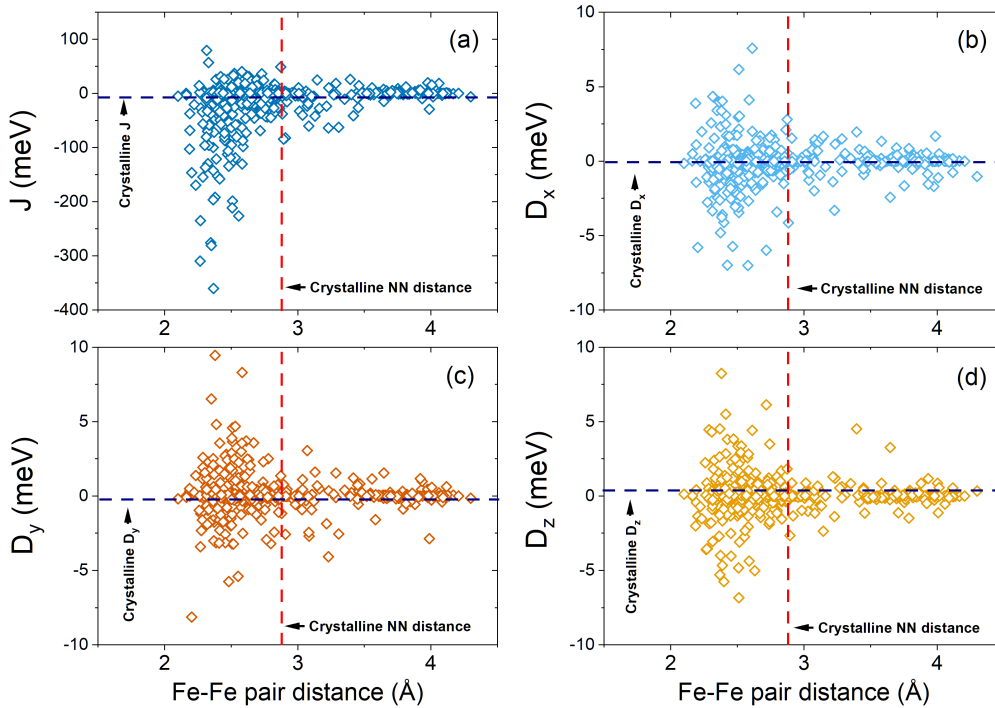


Figure S3. Calculated magnetic exchange couplings (a) and three components of the DMI (b-d) of three amorphous FeGe structures are shown as a function of the Fe-Fe pair distances. The horizontal line references the corresponding 1NN values of the crystalline FeGe structure in Fig.S1 and the vertical line represents the 1NN bond-length of the crystalline FeGe

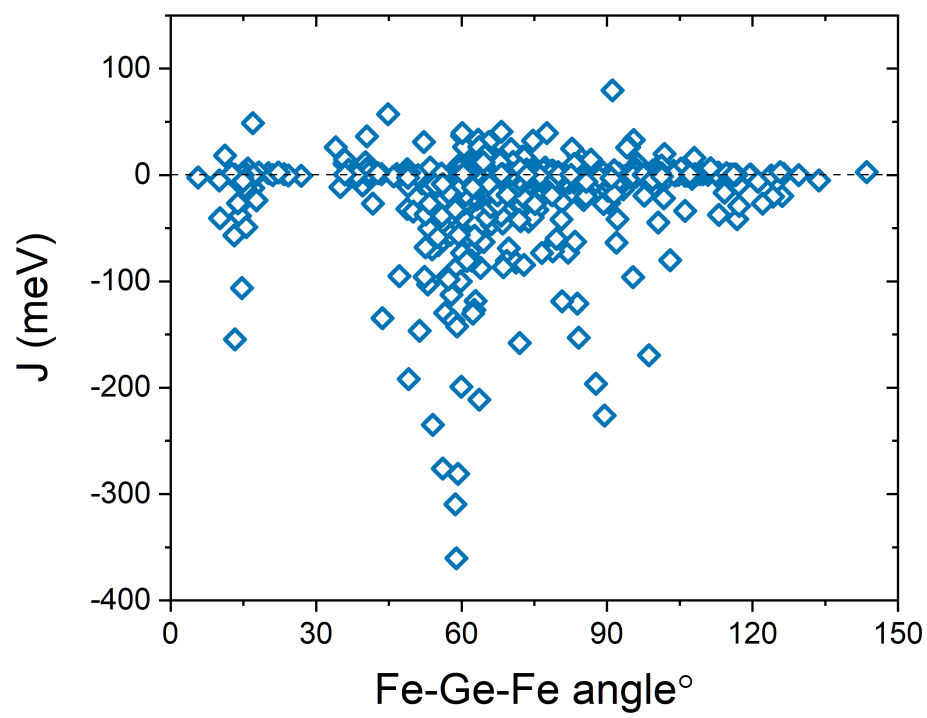


Figure S4. Exchange coupling interactions, J , as a function of the Fe-Ge-Fe angle.